Analysis of the instability conditions and failure mode of a special type of translational landslide using long-term monitoring data: A case study of the Wobaoshi landslide(in Bazhong,China)

Yimin Liu[a,b] , Chenghu Wang[a,*] , Guiyun Gao[a] , Pu Wang[a] , Zhengyang Hou[a] , Qisong Jiao[a]

[a] Institute of Crustal Dynamics, China Earthquake Administration, Beijing, 100085, China

[b] School of Manufacturing Science & Engineering, Sichuan University, Chengdu, 611730 ,China

Abstract: A translational landslide comprising nearly horizontal sandstone and mudstone interbed was widely developed in the Ba river basin of the Qinba–Longnan mountain area. Some progresses on the formation mechanism and failure mode for this type of rainfall-induced landslide have been made in the previous research; however, owing to lack of landslide monitoring data, it is very difficult to demonstrate and validate previously-established geomechanial model. This study considered a translational landslide with an unusual morphology: the Wobaoshi landslide, located in Bazhong city, China. Firstly, the engineering geological conditions of this landslide were ascertained through field investigation, and the deformation and failure mechanism of the plate-shaped sliding body were analyzed. Secondly, long-term monitoring engineering was conducted to obtain multi-parameter monitoring data, such as crack width, rainfall intensity, and pore-water pressure. Finally, based on the geomechanical model analysis of the multi-stage sliding bodies, the equation for the critical water height of the multi-stage plate girders, h_{cr}, was established, and the long-term monitoring data were used to verify its reliability. On the basis of numerical simulation and calculations, the deformation and failure modes of the plate-shaped sliding bodies were analyzed and investigatied. In conclusion,

the multi-parameter monitoring data proved that the stability of the sliding body is controlled

greatly by the rainfall intensity and pore-water pressure and the pore-water pressure in the crack is

positive for the initiation of the plate-shaped bodies sliding, and at the same time, one optimized

monitoring methodology for this type of landslide was proposed. Therefore, this research findings

are of theoretical and practical significance for the intensive study of translational landslides in

this area.

Keywords: Translational landslide; Long- term monitoring; Instability conditions; Failure

mode; Plate-shaped sliding body; Pore-water pressure.

0. Introduction

A special type of landslide occurs in the red beds of the Qinba–Longnan mountainous area.

This landslide is mainly developed in the rock mass of the nearly horizontal sand and mudstone

interbed in the Ba river basin, and it has the following characteristics: the cover layer is extremely

narrow, generally not more than 5 m; the sliding surface is close to horizontal; and the rock layer

inclination angle is generally only 3° - 8°. The sliding body of this landslide is typically a thick

layer of sandstone with good integrity, and its bottom is a weak layer comprising mudstone.

During monsoon, particularly when rainstorms occur, the sliding body is pushed horizontally

along the sliding surface. Some scholars call this phenomenon a flat-push landslide, which is a

typical rainfall-induced landslide (Zhang et al., 1994; Guzzetti et al., 2004; Xu et al., 2010).

Research on the formation mechanism and deformation mode of a translational landslide is

mainly based on two perspectives. The first category includes the translational landslides is

primarily induced by the hydrostatic pressure or confined water pressure resulting from rainstorms

46   (Kong and Chen, 1989; Matjaž et al., 2004; Yin et al., 2005). The sliding body of the thick

47   sandstone can slide along the surface because of the hybrid action of the hydrostatic pressure in

48   cracks and the uplift force of the sliding surface (Wang and Zhang, 1985; Zhang et al., 1994; Xu

49   et al., 2006; Fan, 2007). Simultaneously, the sliding soil, expanded by rain water, causes a slip

50   between nearly horizontal layers (Yin et al., 2005). The second category includes landslides

51   wherein the the upper layer contains hard rock (such as granite and sandstone) has a crushing

52   effect on the lower weak rock layer, thereby causing the rock mass to laterally expand, resulting in

53   a landslide (Cruden and Varnes, 1996; Emelyanova, 1986).

54   Regarding the theoretical study on rainfall-induced translational landslide, scholars

55   worldwide have used physical simulation experiments, gemechanical model analysis, and satellite

56   remote-sensing methods to investigate the genetic mechanism, initiation criteria, and sensitivity

57   analysis of safety factors. Fan et al. (2008) reproduced the deformation and failure process of

58   landslides through physical simulation, and further verified the formation mechanism and

59   initiation criterion formula of the flat-push landslide previously studied by Zhang et al. (1994).

60   Sergio et al. (2006) focused on the influence of pore-water pressure on the stability of

61   rainfall-induced landslides, and studied the soil failure mode based on pore-water pressure via

62   simulation experiment. Floris and Bozzano (2008) and Teixeira et al. (2015) selected rainfall data

63   from historical periodic rainfall conditions, and used physical experiments to establish an

64   optimization model for rainfall-induced landslide initiation criteria for landslides in the southern

65   Apennines and shallow landslides in northern Portugal; they also evaluated landslide susceptibility

66   and safety factors to evaluate the possibility of landslide reactivation induced by rainstorms.

67   Barlow et al. (2003), Martin and Franklin (2005) used US land satellite called enhanced thematic

mapper (ETM+) and digital elevation model (DEM) data to detect the residues of translational

bedrock landslides in an alpine terrain. Bellanova et al. (2018) used resistivity imaging to

investigate the Montaguto translational landslide in the southern part of the Apennines; they also

established a refined geometric model to observe the lithologic boundaries, structural features, and

lateral and longitudinal discontinuities associated with sliding surfaces.

Through the references collation and analysis of the current research status of translational

landslides, scholars worldwide have conducted further research on the formation characteristics

and genetic mechanism of translational landslides. Based on the results of previous studies, the

main focus of this study is on the following two aspects.

(1) The occurrence of plate-shaped translational landslides is often unexpected and covert.

Plate-shaped translational landslides are primarily induced by rainfall; such events often occur in

the red-bed zone of the Qinba–Longnan mountainous area. Due to the dense population and

infrastructures in this area, plate-shaped landslides, characterized by large volumes, and covert

and abrupt occurrence, often cause massive property loss and casualties. In the previous field

investigation, such destructive events are often classified as small-scale rock mass collapses;

hence, the dangers posed by such kind of landslides were easily ignored.

(2) The field investigation and monitoring data for this kind of landslide is often absent. In

the past research, specific geomechanical and physical models have been established using

historical rainfall records, and laboratory physical experiments have been conducted to verify the

failure model (Xu et al. 2006; Fan et al., 2008). However, long-term on-site monitoring data and

related analysis and findings for such landslides have not been reported in publications according

to literature review. Therefore, several key field monitoring parameters, such as width of rear

crack, real-time rainfall, pore-water pressure, and groundwater level, should be obtained to investigate and validate the deformation and failure mode of translational landslides, and be utilized to establish a geomechanical model.

Based on the formation mechanism of the translational landslide established by previous studies, research chosen a typical and specific translational landslide (the Wobaoshi landslide) in the Ba River Basin of the Qinba–Longnan mountainous area, and conducted field investigation, long-term (February 2015 to July 2018) monitoring, geomechanical model analysis, and numerical simulation to investigate the instability conditions and variation failure modes of this translational landslide under the influence of periodic rainfalls.

1. Engineering Geology Characteristics of the Wobaoshi Landslide

1.1. Landslide Location

The Wobaoshi landslide is located in the Ba river basin in the Qinba–Longnan mountainous area. Its specific location is in Baiyanwan village, Sanhui town, Enyang district in Bazhong, China. Fig. 1 presents its geographical location and elevation information. The Wobaoshi landslide is located on the left bank of the Shilong river. The front edge of this landslide is in the curved section of the river, and its left boundary gully is located on the concave bank on the river's left bank. The landslide area is classified as a red-bed layer in a low mountainous area, the vegetation of its sliding body is dense, and its geomorphic unit is cuesta structural slope. The geological structure of the body lies on in the south side of the Nanyangchang anticline, and the landslide involved sandstone and mudstone belonging to the Penglaizhen Formation of the upper Jurassic series (Chen et al., 2015).
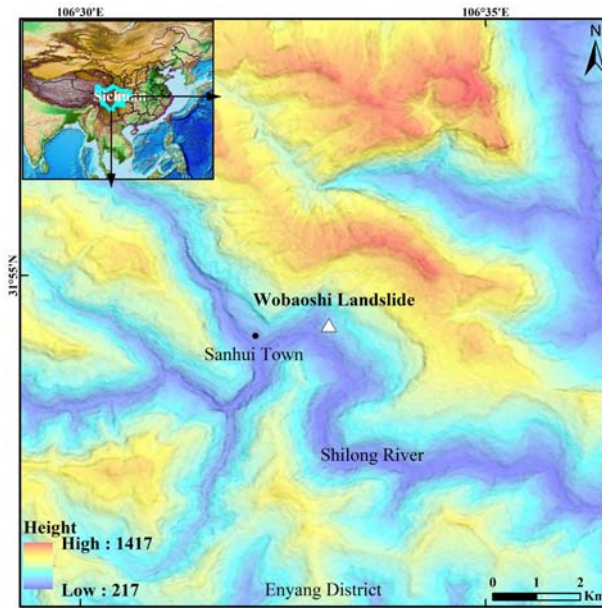
Fig. 1 Geographical location and elevation map of the Wobaoshi landslide.

This landslide is common in the eastern subtropical monsoon climate region, where rainfall is abundant and mostly concentrated from May to October, accounting for 75% - 85% of the total annual rainfall. The monthly average rainfall is above 100 mm, of which the highest occurs in July, the monthly average rainfall in July is over 200 mm and often accompanied by rainstorms, and the rainfall gradually decreases after August in this region (Chen et al., 2015). The types of groundwater are mainly fissure water in weathered bedrock and pore-water in the cracks, and the dynamic change of groundwater is considerably affected by climatic change.

1.2. Landslide Characteristics and Forming Conditions

1.2.1 Engineering Geology Characteristics

According to the satellite remote-sensing interpretation and landslide survey, the shape of the sliding body is a flat long rectangle on the plane. Its longitudinal (sliding) direction is nearly 32 m, the lateral width is 160 m, the average thickness of the sliding body is approximately 30 m, and its volume is approximately 1.536×10^5 m^3 (Chen et al., 2015). This sliding body belongs to small- to medium-sized landslides according to the typical scale. The sliding direction of the landslide is 249°, and the overall attitude of the rockbed is 170° - 180° ∠6° - 8°. The strike in this landslide is nearly parallel to the overall trend of the bank slope, which is a typical nearly horizontal consequent bedding rock slope. Fig. 2 shows a planar graph of the Wobaoshi landslide and photographs of five observation points. Fig. 3 presents I-I$'$ sectional graph of the landslide.
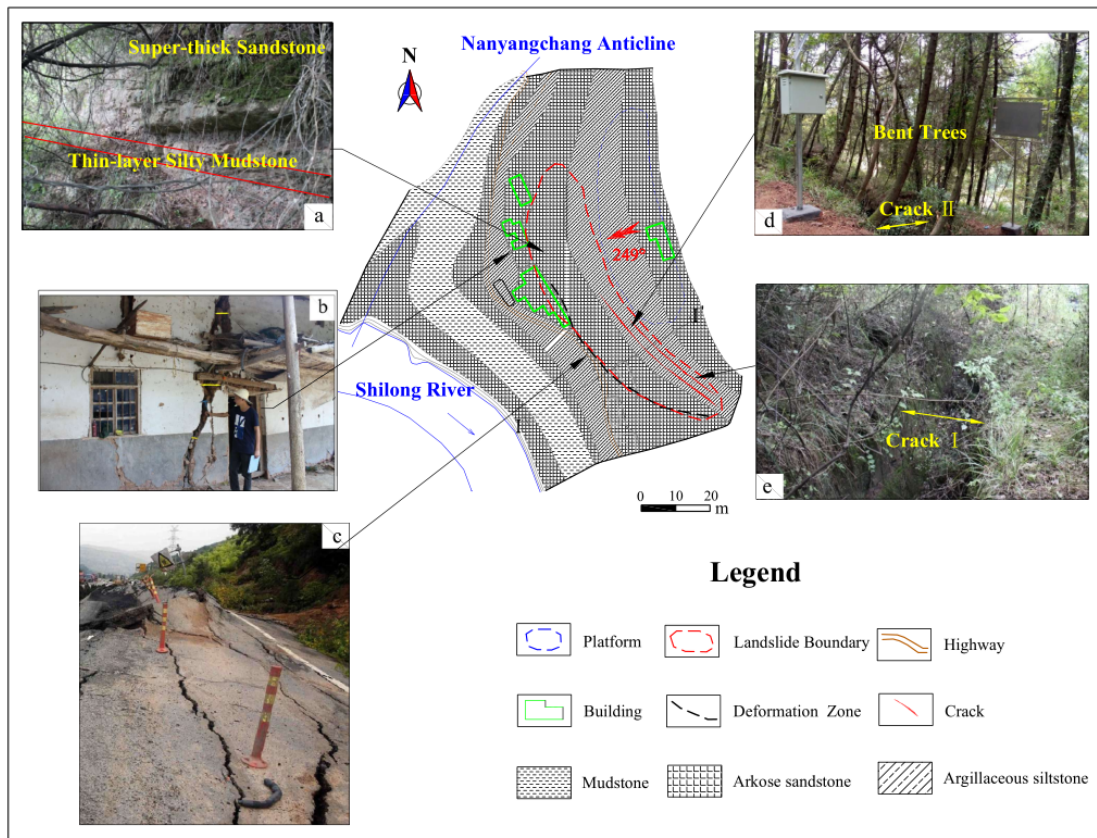
Fig. 2 Topographic map of the Wobaoshi landslide and photographs of observation points: (a) exposed bedrock at the front edge; (b) the houses had cracked at the front edge (c) the roadbed is pushed uplifted at the front edge; (d) crack II and bent trees; and (e) crack I.

Fig. 3 I-I' sectional graph of the landslide
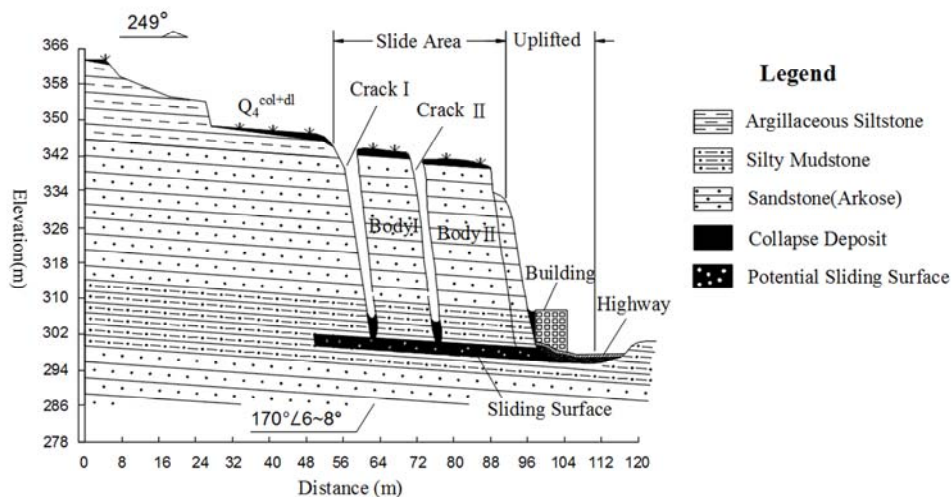
As shown in Fig. 2, the landslide shape is special, the longitudinal length is much less than the lateral width and is even smaller than the thickness of the sliding body. Therefore, this body can be easily mistaken for a multistage dangerous rock mass with deformation during disaster

investigation. According to Fig. 3, the sliding bodies are almost perpendicular to the potential sliding surface, and a group of long and straight structural planes parallel to the slope cut the slope into two narrow plates (sliding bodies I and II); furthermore, the structural surface of the body has a certain degree of aperture, both sides of the crack are closed, and the bottom of the crack is filled with clay in addition to gravel and collapse debris.

1.2.2 Forming Conditions of the sliding bodies

The sliding body of the Wobaoshi landslide formed two obvious cracks from the outside to the inside, which cut and disintegrated the sliding body into plate-shaped blocks from front to back, as shown in the photographs of observation points c and d in Fig. 2. Then, the plate-shaped sliding bodies I and II were formed. The landslide is a two-stage translational landslide in which the longitudinal length of sliding body I is 12 m, the identifiable lateral width is ~ 70 m and the thickness is ~ 30 m, the longitudinal length of the sliding body II is 16 m, the identifiable lateral width is ~ 65 m, and the thickness is ~ 28 m. Sliding body I forms crack I with the trailing edge of the landslide, and sliding body II forms crack II with sliding body I. When large rainfall intensity occurs during monsoon, the pore-water in the cracks can be observed, thus indicating that cracks I and II have preferable water-storage conditions.

As the photograph of observation point d in Fig. 2 shows, bent trees grow on the trailing edge of landslide bodies I and II. The trees on the landslide are skewed with the soil mass sliding, and after the sliding stops, the upper part of the trunk turns to the upright state year by year. The existence of bent trees represents the tendency of the slope body to become unstable or the existing landslide accumulation body tends to slide again, this is also historical evidence of the slow sliding of the landslide (Zhang et al., 2015).

As the photo of observation point a in Fig. 2 shows, the shallow surface of the Wobaoshi landslide is a 2–3 m thick layer of collapsed and plowed soil. The sliding body contains extremely thick sandstone with good integrity, and the bottom sliding surface is a weak interlayer comprising of silty mudstone. In summary, the Wobaoshi landslide is a typical and special translational landslide, and based on the characteristics of its plate-shaped body, it can be considered a plate-shaped landslide (Fan et al., 2008; Xu and Zeng, 2009).

The engineering geological conditions of the Wobaoshi landslide are inferred on the basis of

175 its characteristics; i.e., the rapid immersion of groundwater softens the joint surface of soil and

176 rock formation, especially under a rainstorm. Then, the group of open cracks parallel to the slope

177 in the sliding body is concentrated and quickly filled with water, following which groundwater

178 level rises and the pore-water pressure increases sharply, such that the sliding bodies I and II will

179 slide along the contact surface of the bottom sand-mud-rock weak layer. This condition changes

180 the stress mode and equilibrium state of the rock and soil mass, thereby easily inducing a landslide.

181 As shown observation point b and c in Fig. 2, the Wobaoshi landslide seriously threaten

182 residential houses and highways, the houses had cracked and highways had uplifted on its front

183 edge, so this landslides seriously threatens the safety of people's property and transportation.

184

2. Landslide Monitoring Scheme and Monitoring Data Analysis

2.1. Long-term Monitoring Scheme

187 According to the detailed investigation of the Wobaoshi landslide, two cracks extend through

188 the sliding surface at the trailing edge of the landslide, and the pore-water in the cracks exists

189 during periodic rainfalls. As the hydrostatic pressure in the cracks strongly influences the stability

190 of the plate-shaped landslide (Fan et al., 2008; Guo et al., 2013), via real-time monitoring of

191 cracks, rainfall and pore-water pressure measurements were conducted from February 2015 to

192 July 2018 to determine the landslide state in different periods such as rainy and non-rainy seasons,

193 together with the interaction between multilevel plate girders and sliding surface. Fig. 4 shows the

194 layout graph of the monitoring equipment.

195
196   Fig. 4 Layout planar graph of the monitoring equipment
197
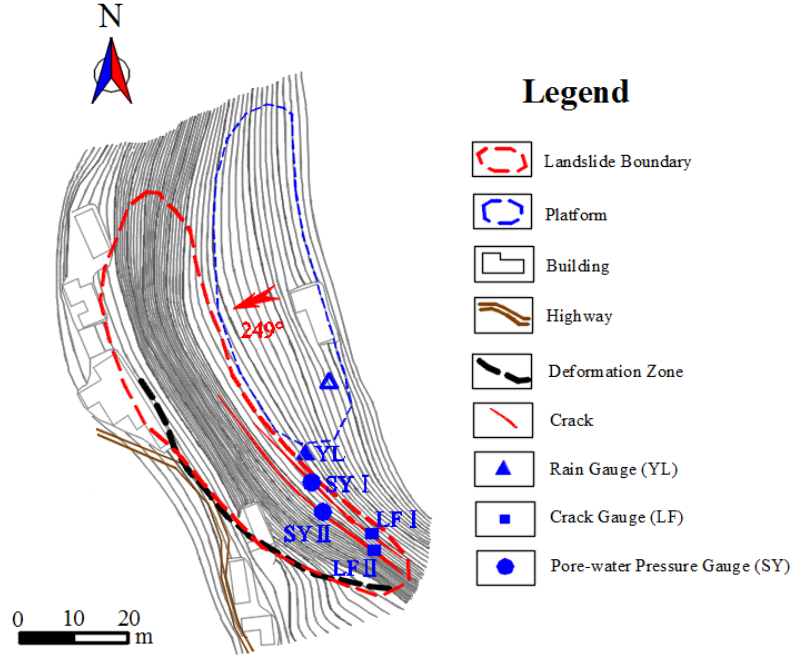
198   As shown in Fig. 4 shows, two non-contact crack automatic monitors, LF I and II, are

199   installed on both sides of cracks I and II, respectively, to record real-time variation of the width of

200   the two cracks (Liu et al., 2015). An automatic rain gauge is installed in flat space and no tree

201   occlusion is observed at the trailing edge of the landslide to record real-time and cumulative

202   values of the rainfall. Two pore-water pressure gauges are installed at the bottom of crack I and II

203   to measure the pore-water pressure. The value of pore-water level, h_c, can be calculated using the

204   relation $h_c = H - h_i + h_m$, where hi is the installation depth of the pore-water pressure gauge; H is

205   the depth of the crack; and h_m is the measured value of the pore-water pressure gauge.

206   In this example, the initial width value of crack I is 5.640 m, and the initial width value of

207   crack II is 4.492 m (the first measurement was conducted in January 2015); the installation depth

208   $h_{i1} = 24.72$ m, and the depth of crack I is $H_1 = 38$ m, with $h_{c1} = 13.28m + h_{m1}$. Additionally, the

209   installation depth $h_{i2} = 24.85$ m, and the depth of crack I is $H_2 = 35$ m, and $h_{c2} = 10.15m + h_{m2}$.

210   The monitoring frequency of the crack width is thrice a day, the monitoring frequency of the

211   pore-water pressure is twice a day, and the rainfall intensity adopts the accumulative value of one

212   month. The multiparameter monitoring data are transmitted to the monitoring server through the

213   GPRS network.

(a)   (b)   (c)
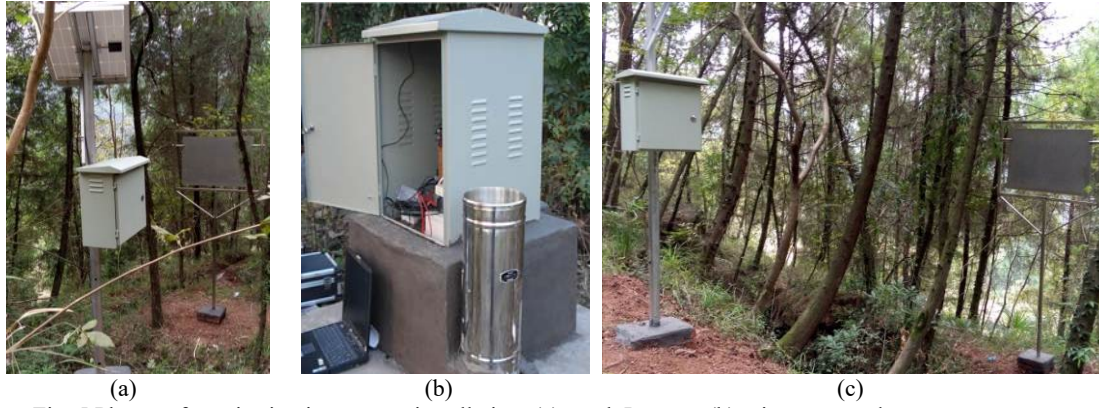
Fig. 5 Photos of monitoring instrument installation: (a) crack I gauge; (b) rain gauge and pore-water pressure gauge; (c) crack II gauge.

2.2. Monitoring Data Analysis

By the monitoring work performed on the Wobaoshi landslide for three-and-a-half years (February 2015 to July 2018), this study selected the typical data of the width of cracks I and II, the pore-water pressure and the rainfall intensity, details of these monitoring data are in listed in Tables 1 and 2. The corresponding time curves in Fig. 6 show the monitoring data of the rainfall intensity and the width of cracks I and II. Fig. 7(a) and 7(b) present comparison curves of the monitoring width data of cracks I and II against their pore-water pressures, respectively.
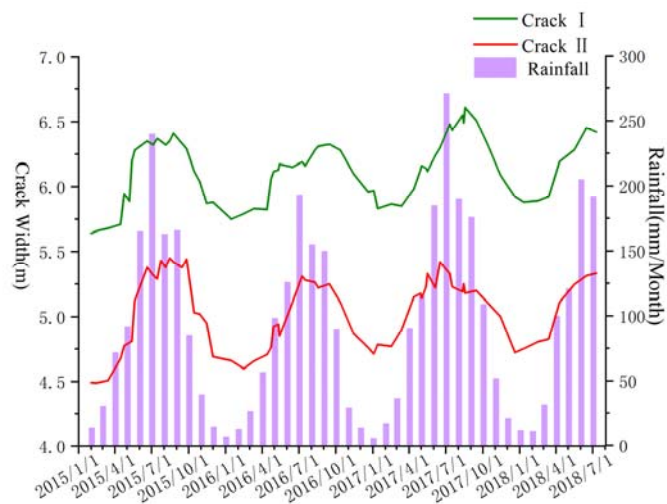
Fig. 6 Monitoring data curves (rainfall intensity and width of cracks I and II)
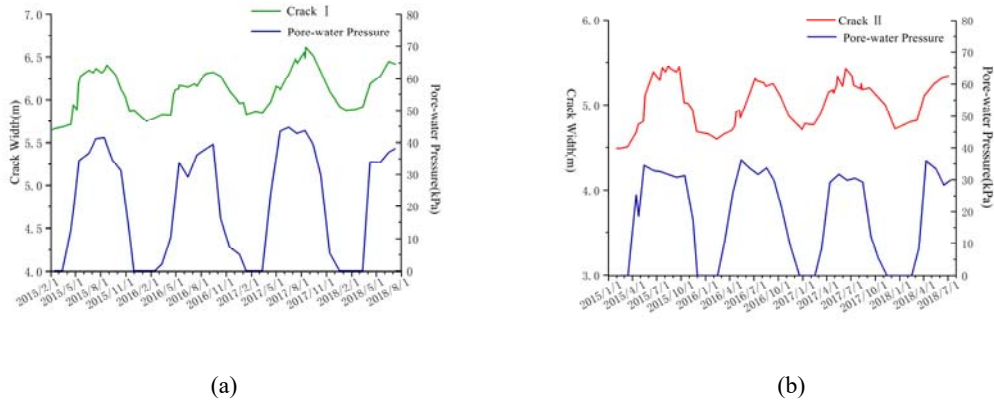
(a) (b)

Fig. 7 Monitoring data curves: (a) width of crack I and its pore-water pressure; (b) width of crack II and its pore-water pressure.

Based on the comprehensive comparison and analysis of the data curves presented in Figs. 6 and 7, this study concludes that the Wobaoshi landslide is still in creep deformation state, and the plate-shaped sliding body exhibits a regular trend with changes in rainfall intensity and pore-water pressure. Cracks I and II show a preferable water-storage capacity during monsoon, and increasing pore-water pressure affects the crack width variation. The specific analysis is as follows.

(1) A clear correspondence exits between the absolute amount of crack width change and season change (i.e. change in rainfall intensity); the magnitude of the rainfall intensity determines the change of the width of the two cracks. As shown in Fig. 6, the widths of cracks I and II widen as the rainfall intensity increases during monsoon (May to September), and their crack widths gradually decrease as the rainfall intensity lowers during the non-rainy seasons (October to April in the next year). As indicated in Fig. 8, the maximum width of crack I reaches 6.615 m, and the absolute stretching amount of this crack is close to 1 m in the July–August period in 2017 (monthly rainfall exceeding 250 mm). The maximum width of crack II is also in the range of 5.40–5.45 m, and its absolute stretching amount exceeded 1 m during July–August 2015 and

July–August 2017. During non-rainy seasons, when the rainfall intensity lowers, the crack width

begins shrinking, and it decreases to its minimum in January in each monitored year.
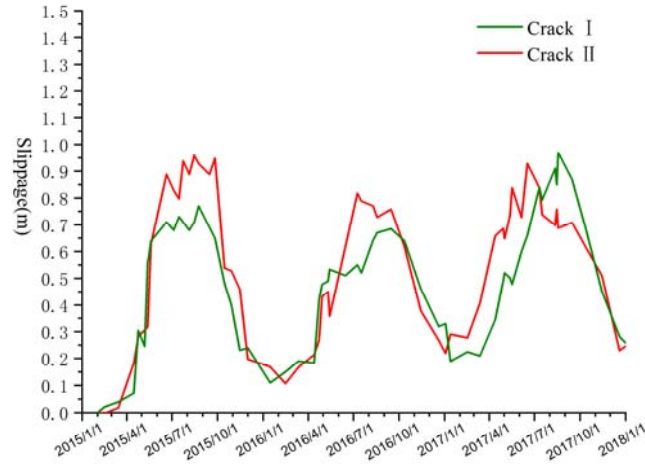
Fig. 8 Absolute slippage amount curves of crack I and II

(2) The width of cracks I and II tend to increase year by year, indicating that the two-stage

sliding body of the Wobaoshi landslide is still moving along the sliding surface because of the

influence of rainfall. In Fig. 6, the measured data in the monitoring period indicate that the

minimum widths of crack I and II are gradually increasing, and their maximum value is

considerably affected by the rainfall intensity of a particular month.

(3) Fig. 7 shows that the stretching of cracks I and II, or both follows the same trend as the

pore-water pressure, i.e., the magnitude of pore-water pressure determines the width variation of

the cracks. Fig. 7 also shows that the water-storage capacity of crack I is good during monsoon,

and after the sliding body slides, it can maintain a certain pore-water level because of rainfall

replenishment. Additionally, the increase in rainfall intensity increases the water level in the

cracks, and the increase in pore-water pressure positively affects the initiation of the plate girder.

The curve in Fig. 8 shows that the increase in pore-water pressure has a significant causal relationship with the stretching of the cracks.

3. Model Calculation and Numerical Simulation

To construct a generic model of the evolution process of the Wobaoshi landslide, a geomechanical model of plate-shaped sliding bodies was established, its stability was calculated,and it was combined with monitoring data for a comparative analysis. According to previous findings(Fan, 2007; Fan et al., 2008; Xu et al., 2010), when many penetrating cracks are parallel to the slope in the rock mass, and these cracks are filled with water, the water pressure on both sides of each plate-shaped body attains in a balanced state except for the outermost body. However, once the outer body slides, owing to the sudden decrease of the pore-water level in the trailing edge crack, the water pressure around immediately following plate-shaped body becomes unbalanced, and new sliding damage is induced (Fan, 2007; Xu et al., 2010).

3.1. Model Establishment and Stability Calculation

According to characteristics of the Wobaoshi landslide in Section 1.2, when the geomechanical model is established, the cover layer is neglected, and the static geomechanical model of the plate-shaped rock sliding body is established based on the limit equilibrium method. The basic characteristic of the limit equilibrium method is that the Mohr-Coulomb failure criterion of the soil in static equilibrium conditions is considered, that is, the problem's solution is solved by analyzing the destruction of the soil's balance. And the soli elastic-plastic ideal model was chosen, which obey the Mohr-Coulomb failure criterion and associated flow rules (Darve and Vardoulakis, 2004; Labuz and Zang, 2015).

For the failure mode of the two-stage plate girders of the Wobaoshi landslide, this study selected a typical section of plate-shaped sliding bodies and established the geomechanical model, shown in Fig. 9 In this section, first, a stability analysis of the outer layer plate girder II, is conducted and then the inner plate girder I is analyzed.
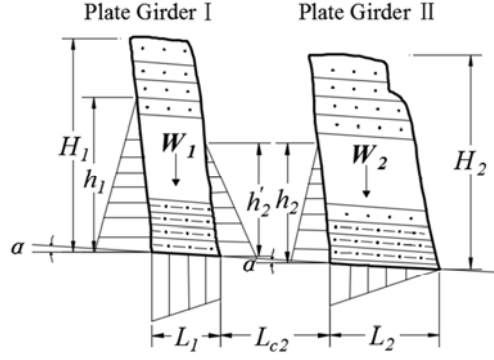
 Fig. 9 Geomechanical model of two-stage plate-shaped sliding bodies

In Fig. 9, α is the angle of the sliding surface, h_1 and h_2 are the heights of the pore-water

levels in cracks I and II, respectively; L_1 and L_2 are the widths of plate girders I and II, respectively;

L_{c2} is the distance between plate girder I and II; H_1 and H_2 are the heights of plate girders I and II;

respectively, and W_1 and W_2 are the self-weights of plate girders I and II per unit width,

respectively. According to the relationship between the stability coefficient of plate girder, K, and

the height of the pore-water level, h, shown in Fig. 7 (Zhang et al., 1994; Xu et al., 2010), while

considering the internal cohesive force of the sliding surface, the equation to calculate the stability

coefficient, K_2, of the outer layer plate girder II is expressed as follows:

$$K_2 = \frac{\left(W_2\cos\alpha - \dfrac{1}{2}\gamma_w h_2 L_2 - \dfrac{1}{2}\gamma_w h_2^2\sin\alpha\right)\tan\theta + cL_2}{\dfrac{1}{2}\gamma_w h_2^2\cos\alpha + W_2\sin\alpha}. \tag{1}$$

In Eq. (1), c is the internal cohesion of the sliding surface; γ_r is unit weigth of the saturated

volume of the sandstone; γ_w is unit weight of water; and $W = H\cdot L\cdot\gamma_r$. K_2 is set to 1, i.e., the plate

girder II is set in a critical sliding state (GB/T 32864-2016, 2017). Then Eq. (2) of the maximum

pore-water level of plate girder II, h_{cr2}, is derived from Eq. (1).

308
$$h_{cr2} \approx \frac{1}{2 \cos \alpha} \left[L_2^2 \tan^2 \theta + \frac{8}{\gamma_w} \left(W_2 \cos \alpha \tan \theta - W_2 \sin \alpha + cL_2 \right) \cos \alpha \right]^{\frac{1}{2}} \quad (2)$$
$$- \frac{L_2}{2 \cos \alpha} \tan \theta$$

309 According to the experimental data of the triaxial test of the Wobaoshi landslide's rock core

310 (Chen et al., 2015), the internal friction angle of the sliding surface is $\theta = 11.2°$, unit weigth of the

311 saturated volume of the sandstone is $\gamma_r = 19.2$ kN/m^3, unit weight of clear water is $\gamma_w = 9.8$ kN/m^3,

312 and the internal cohesion of the sliding surface is $c = 10.2$ kPa. According to the sectional graph of

313 the Wobaoshi landslide (see Fig. 2), $H = 35$ m, $L = 16$ m, and $\alpha = 6°$. Therefore, according to Eq.

314 (2), $h_{cr2} = 13.896$ m.

315 Based on the stability analysis of plate girder II, combined with Eq. (1), Eq. (2), and Fig. 7,

316 the equation to calculate the stability coefficient K_I of the inner layer plate girder I can be

317 expressed as Eq. (3). In addition, $h_2' = h_2 - L_{c2} \sin\alpha$ and $L_{c2} = 3.8$ m; therefore, $h_2' = 13.499$ m.

318
$$K_1 = \frac{\left[W_1 \cos \alpha - \frac{1}{2} \gamma_w \left(h_1 + h_2' \right) L_1 - \frac{1}{2} \gamma_w \left(h_1^2 - h_2'^2 \right) \sin \alpha \right] \tan \theta + cL_1}{\frac{1}{2} \gamma_w \left(h_1^2 - h_2'^2 \right) \cos \alpha + W_1 \sin \alpha} \quad (3)$$

319 Similarly, K_I is set to 1 and, in plate girder I, $H_I = 38$m, $L_I = 12$m, $\alpha = 6°$, $h_2' = 13.499$m,

320 therefore, the maximum pore-water level h_{cr1} of plate girder I can be calculated using the Eq. (3)

321 and $h_{cr1} = 17.249$m.

322 The preceding calculation results show that, when the pore-water level at the trailing edge of

323 the plate girder reaches the maximum height at which the landslide begins, i.e., when $h_{cr1} =$

324 17.249m and $h_{cr2} = 13.896$m, the pore-water pressure triggers the plate-shaped sliding bodies. In

325 next section, the pore-water monitoring data, which were acquired via the landslide monitoring are

326 used to verify the equation.

327 The pore-water monitoring data in Section 2.2, which were acquired via the landslide

328 monitoring engineering, were used to test the equation for calculating the maximum height of

329 multistage plate girders, h_{cr}. According to the monitoring data of the pore-water pressure and the

330 installation depth of the sensors, the actual calculated maximum height values h_{c1} and h_{c2} of the

331 pore-water level are presented in attached Table 3. Combined with the change in the absolute

332 stretching amount in Fig. 8, typical data of the measured pore-water level are selected,

333 corresponding to the sudden increase in the absolute slippage (see Table 3 for details), as shown in

334 Fig. 10.

335

336   (a) Crack I   (b) Crack II

337   Fig. 10 Determination of the maximum measured pore-water level $h_{cr}^{'}$

338
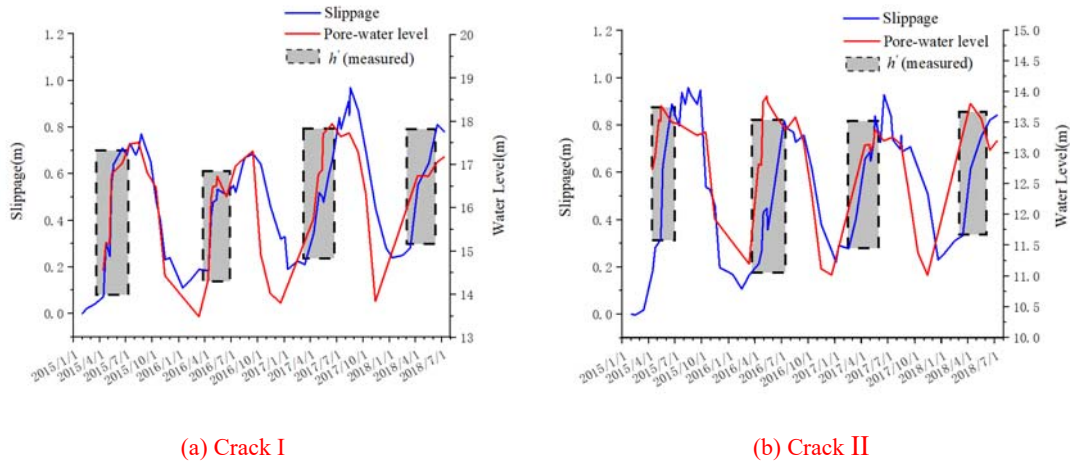
339 The dotted boxes in Fig. 10 represent the value of the pore-water level when the bodies are

340 sliding, i.e., the maximum pore-water level, $h_{cr}^{'}$, which causes the sliding body to be unstable. The

341 measured $h_{cr}^{'}$ in Fig. 10 can be compared to the relationship between the pore-water level, h, and

342 the stability coefficient of the plate girder, K, in equation (1) and (3), which are also shown in Fig.

343   11.

344

345   (a) Crack I   (b) Crack II
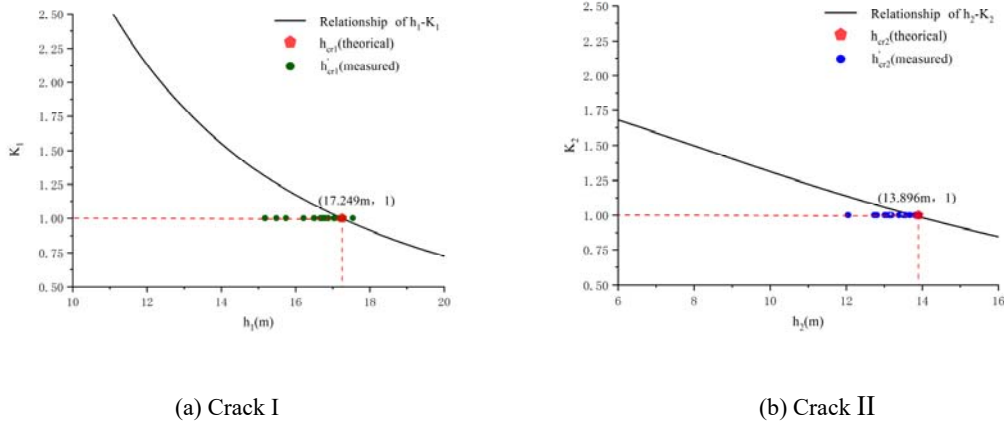
346   Fig. 11 Comparison of $h_{cr}^{'}$(measured) and h_{cr} (theoretical)

347

348   In Fig. 11, the curves of the h-k relationship represent equations (1) and (3). The values of $h_{cr}^{'}$

349   (measured) in Fig. 11 show that most of the monitoring pore-water levels are not higher than those

350   theoretically calculated. The Wobaoshi landslide monitoring example shows that in most cases,

351   when $h_{cr}^{'}$(measured) $\leqslant$ h_{cr} (theoretical), the pore-water pressure causes the instability of the

352   sliding body.

353   **3.2. Numerical Simulation of the Plate-shaped Sliding Bodies**

354   The numerical simulations and calculations of the plate girder were performed using MIDAS

355   GTS NX geotechnical finite element software. First, the 1:1 sliding body model in Fig. 9 was

356   introduced into the finite element software, and the mechanical parameters of the sliding body

357   model, i.e., elastic modulus, Poisson's ratio, gravity internal cohesion and friction angle, were

358   defined as shown in Table 4. The position of the right side of the landslide about 30m from the

359   foot of the slope is selected as the right boundary of the model; the lower boundary is setted at the

360   elevation of 0 m; the left boundary is located inside the mountain, about 30m away from the plate

361   girder I. The element type adopts a plane strain quadrilateral-triangle mixing element, and the

362   whole model is divided into 13775 elements and 14026 nodes. Here we constrain the vertical and

363   horizontal displacement of its bottom boundary, and the left and right boundary conditions are set

364   to constrain the horizontal displacement. The model uses steady-state seepage calculation, and the

365   water levels at the left and right boundaries were set to 342 and 275 m, respectively. The boundary

366   conditions are set as follows.

367   (1) For the displacement boundary, the left and right boundaries constrained the displacement

368   in the X-direction; i.e., TX = 0. For the bottom boundary, the displacement in the X and Y

369   directions was constrained; i.e., TX = TY = 0.

370   (2) For the seepage conditions, the water levels at the left and right boundaries were set to

371   342 and 275 m, respectively.

372   The typical pore-water-level data of the 4 cycles from 2015 to 2018 in the crack I and crack

373   II presented in Table 3 and Fig. 10 were introduced into the finite element model, and were

374   selected for a typical cycle change period presented in Table 5, followed by numerical calculations

375   to obtain the typical deformation and displacement states of plate-shaped sliding bodies in the

376   rainy and non-rainy seasons, as shown in Fig. 12.

377

379   (a) The Initial state   (b) Sliding bodies occur when pore-water level increase

381   (c) The sliding bodies slide to the maximum state   (d) Sliding bodies tilt backward when water level decreases

382   Fig. 12 Example of finite element simulation and numerical calculation

383
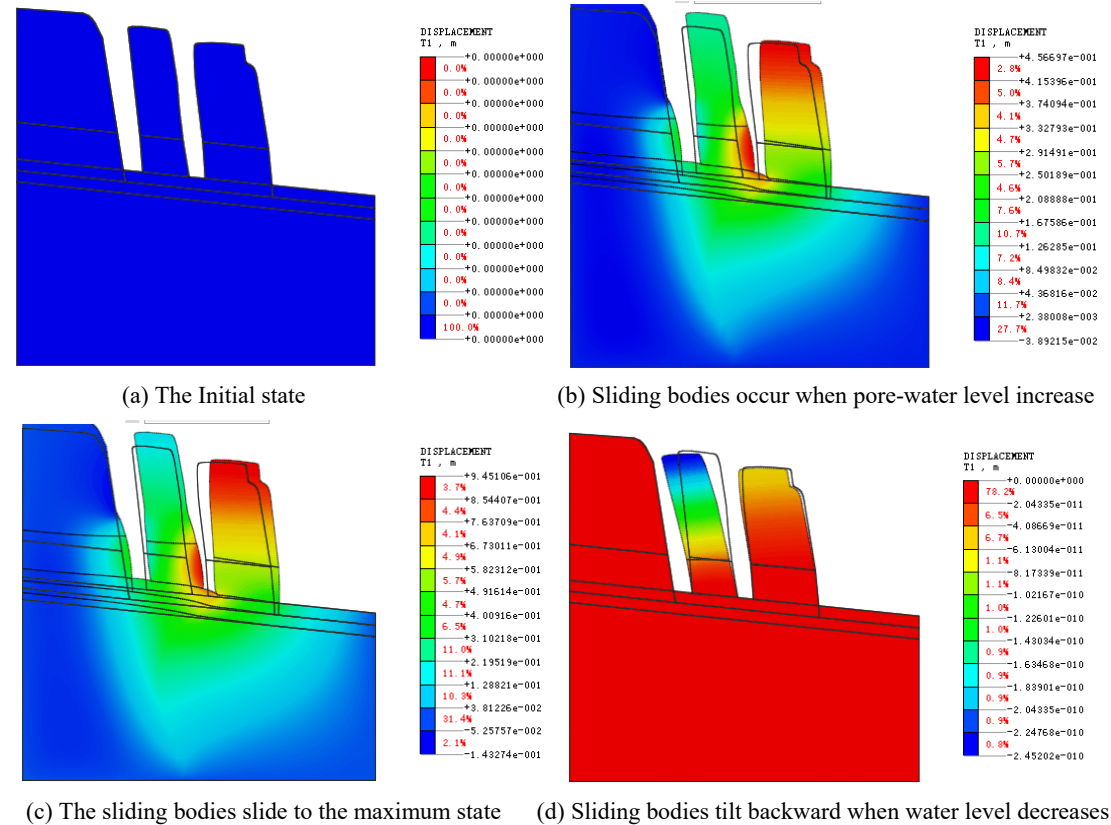
384   The initial displacement state in Fig. 12(a) is set to zero for the following analysis. Fig 12(b)

385 shows that, under the combined effect of the pore-water pressure and seepage, the multistage plate

386 girders slide horizontally along the sliding surface. In Fig. 12(c), the multistage plate girders have

387 slid to the maximum distance, where the maximum distance of slider II is 0.945 m, which is close

388 to the value obtained in the monitoring data. In Fig. 12(d), owing to the decrease in pore-water

389 level in the non-rainy season, sliding bodies I and II have the same tendency to tilt backward.

390 Therefore, the calculation results of the numerical simulation can corroborate the sliding-body

391 mechanics model and the landslide monitoring data.

392

4. Discussion

394   According to the traditional theory of granular equilibrium limit, deformation or sliding

395 movement of this nearly horizontal bedrock slope is nearly impossible, and the likelihood of

396 forming a landslide is minimal. However, this special structure of translational landslide widely

397 occurs in the Qinba–Longnan mountainous area during the investigation of geological hazard

398 hidden dangers. Therefore, in the investigation and risk assessment of geological hazards, the

399 characteristics of the plate-shaped landslide and the deformation and failure mode should be

400 combined to detect the hidden dangers with the geological conditions of the landslide. Combining

401 the results of previous studies with those of the monitoring, the discussion herein is divided in the

402 following three parts.

4.1. Deformation and Failure Mode Exploration of the Wobaoshi Landslide

404   The monitoring results of the Wobaoshi landslide in this case validate the rainfall-triggered

405 failure mode of the translational landslide (Zhang et al., 1994). According to the landslide

406 monitoring data, particularly the change trend of the cracks opening and closing in Section 2.2,

407 and the numerical simulations of the plate-shaped sliding bodies in Section 3.2, the deformation

408 and failure mode of the landslide were obtained, as shown in Fig. 13. Fig. 13 shows the

409 deformation of the plate-shaped sliding bodies in the Wobaoshi landslide during the monitoring

410 period (non-rainy season–rainy season–non-rainy season). As shown in Fig. 13(b), the large

411 amount of rainfall in monsoon causes the cracks to be filled with water; when the pore-water level

412 reaches the maximum height at which the landslide begins, the increased pore-water pressure

413 positively affects the initiation of the plate-shaped sliding body (Fan et al., 2007). When the

414 pore-water pressure rises to the threshold value, the plate-shaped landslide can be triggered. In this

415 monitoring case, the pore-water pressure can push the plate-shaped sliding body by nearly 1 m,

416 resulting in the uplift of residential houses and highways on its leading edge. Therefore, we can

417 infer that one or more penetrating cracks are likely parallel to the slope in the body. With the

418 approach of the rainy season, the plate-shaped sliding body II begins to slide first and the water

419 pressure balance in the cracks is destabilized. This condition causes the gliding of the plate-shaped

420 sliding body I, thus forming a multistage translational landslide with characteristic step-by-step

421 backward movement.

422 (a) Initial State of Plate Girder   (b) Sliding in Rainy Season   (c) Tilting in Dry Season
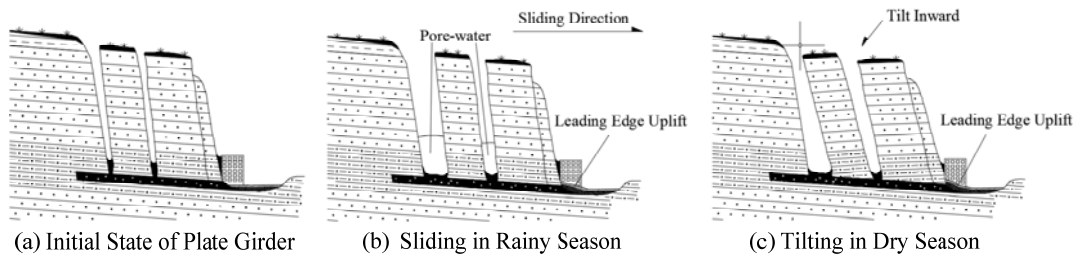
423 Fig. 13 Schematic of deformation and failure mode of the Wobaoshi landslide

424

425 As shown in Fig. 13(c), the plate girder is tilted to the trailing edge by the lower pore-water

426 level and its own weight with less rain during the non-rainy season, thereby causing the plate

427 girder to fall backward (inside the slope) until the top of the plate girder is in contact with the

428 slope surface, the crack width begins shrinking, and a narrow A-shaped crack is formed.

429 Monitoring data of the Wobaoshi landslide and numerical simulation of plate-shaped sliding body

430 also verify the deformation and failure mode of the plate-shaped landslide post landslide

431 occurrence (Xu et al., 2010). Year after year, the cracks at the bottom of the slab-shaped sliding

432 body grow larger, and the degree of inclination of the plate girder continues to increase. The

433 degree of arching of the front edge also increases, which causes the stability of the landslide to

decrease continuously, thereby posing a high risk for the houses and roads on the front edge of the landslide.

4.2. Determination of Maximum Pore-water Level h_{cr}

The theoretical analysis and stability calculation of the geomechanical model of the plate girder is described in Section 4.1, together with the initiation criterion for multistage sliding bodies of translational landslide, i.e., determination of the maximum water height in the crack, h_{cr}, (Zhang et al., 1994) and calculation of the sliding body's stability coefficient, K, (Xu et al., 2010), which is determined by the theoretical calculation of strata inclination, shape, weight, and physical properties (such as unit weigth of the saturated volume, γ_r, internal cohesion of the sliding surface, c, and internal friction angle of the sliding surface, θ) based on the limit equilibrium theory (Lin et al., 2010). Therefore, the stability coefficient of the landslide exponentially decreases with the increase in the water-filling height of the trailing edge crack (Fan, 2008; Xu et al., 2010).

The internal friction angle, $\theta = 11.2°$, is so low for clay, which seems unrealistic. However, the angle θ is obtained by triaxial compression tests of the core, which is taken from the sand-mudstone contact surface in sliding surface, and the internal friction angle $\theta = 11.2°$ (Chen et al., 2015). One of the reasons may be that the clay layer is severely weathered, so its internal friction angle is small. In general, the dilatancy effect obtained by the associated flow law is much larger than the actual observation, especially in the case of lateral confinement (Tschuchnigg et al., 2015a). However, for slope stability analysis, laternal infinite is not considered in most cases, and the dilatancy effect is not significant (Griffiths & Lane, 1999). Therefore, it is reasonable to set the dilatancy angle to be equal to the internal friction angle.

In this case, in the equation for calculating the maximum pore-water level, h_{cr}, deduced in Section 3.1, comparing the measured data of the Wobaoshi landslide in Section 2.2, we can observe that the measured maximum pore-water level, $h_{cr}^{'}$, is close to the theoretical maximum pore-water level, h_{cr}, thus validating the calculation equation of h_{cr}, and the instability conditions of the sliding bodies. Additionally, the most measured data in Tab. 3 are slightly smaller than the theoretical calculation value, i.e., $h_{cr}^{'} \leq h_{cr}$. Thus, compared with the calculation equation of the

461 maximum water height proposed by Zhang et al. (1994) and the physical simulation experiment

462 conducted by Fan et al. (2008), the monitoring case of the Wobaoshi landslide shows that the

463 measured data $h_{cr}^{'}$ is mostly lower than the theoretical calculated value, h_{cr}, which can cause

464 instability of the sliding body. The reason for this instability may be that the actual cohesion value

465 c' of the sand-shale contact surface is smaller than the cohesive force value c of the sliding surface

466 in equation (2) during the creep state of the landslide for a long duration or that the frictional angle

467 of the sliding surface, θ, changes slightly. According to the calculation of the stability coefficient,

468 K, in equation (2), when $c' \leq c$, $h_{cr}^{'} \leq h_{cr}$ is obtained, the plate girder slides in the case wherein $h_{cr}^{'}$

469 (measured) is not larger than h_{cr} (theoretical).

4.3. Optimization Methods of Landslide Monitoring

471   Focusing on the plate-shaped translational landslide through the existing field monitoring

472 result experience and deformation and failure mode exploration, this study proposes the long- term

473 monitoring method with more parameters referring to the characteristics of suchlandslides.

474   First, long- term monitoring should be conducted to obtain sufficient monitoring data, which

475 mainly includes obtaining groundwater level, pore-water pressure, rainfall intensity, and

476 displacement data on the front edge of the landslide during monsoon, as well as focusing on the

477 change of overall inclination of the plate girder during the non-rainy season. This is because the

478 inclination angle α relative to the sliding surface also changes after the sliding of the plate girder.

479 Thus, the inclination measuring device which consists of three-axis accelerometer and electronic

480 compass should be installed in the sliding body, to verify the theoretical exploration of

481 deformation mode of the plate-shaped sliding body in the non-rainy season in Fig. 13(c).

482 Furthermore, a sensitivity analysis of various parameters affecting the stability coefficient K of the

483 sliding body (such as the pore-water level, internal cohesive force in saturated water, internal

484 friction angle of the sliding surface, and inclination angle of the plate girder) should be conducted

on the basis of the monitoring data. Therefore, an in-depth analysis and exploration of the deformation and failure mode of the plate-shaped landslide would be beneficial and would improve the success rate of landslide warning.

5. Conclusions

Considering the case of the Wobaoshi landslide as an example, this study uses research methods such as field exploration, a long- term monitoring engineering, geomechanical model analysis and numerical simulation to deeply analyze the instability conditions and failure characteristics of a special type of translational landslide. The research results are beneficial to the stability analysis and evaluation of this type of landslide. Targeted monitoring methods are proposed to enrich theoretical research on the translational landslide. The following conclusions are drawn:

(1) The characteristics, formation conditions, and occurrence mechanism of rainfall-triggered translational plate-shaped landslides are summarized herein. Such landslides generally exists in a consequent slope with the inclination angle of the sliding surface being less than 10°, and a group of long and straight structural planes parallel to the slope cuts the slope into several narrow plates. The plate-shaped sliding body generally contains extremely thick sandstone, which is nearly horizontal and has good integrity. The bottom sliding zone is a weak mudstone interlayer affected by periodic rainfalls. In addition, single-stage or multistage plate-shaped sliding bodies slide horizontally along the bottom mudstone sliding zone.

(2) Based the mechanical model of the plate-shaped sliding bodies, the relationship between

the stability coefficient of the multistage sliding body, K, and the pore-water level, h, was obtained,

and the maximum pore-water level, h_{cr}, which causes the instability of multi-stage plate girders

was calculated. The instability conditions of the plate-shaped sliding bodies were also determined.

(3) Theoretical conclusions of the plate-shaped landslide research were verified using the

long-term monitoring data. The multiparameter monitoring data show that the stability of the

sliding body is considerably affected by the rainfall intensity and pore-water pressure. The

pore-water pressure in the crack is positive for the beginning of the plate-shaped sliding body,

which demonstrates the rainfall-triggered failure mode of the translational landslide. This study

compares and analyzes the measured maximum pore-water level h_{cr}' and theoretical calculated

value h_{cr}, and discusses the influence in the change of internal cohesive force and internal friction

angle on the stability coefficient of the sliding body.

(4) Combined with landslide numerical simulation, this study analyzes and explores the

deformation and failure modes of the plate-shaped landslide, i.e., combined with the pore-water

pressure in the crack and seepage effect in monsoon, the sliding bodies will slide horizontally

along the contact surface of the bottom sand-mud rock weak layer. During the non-rainy season,

the pore-water pressure decreases and disappears; the sliding body, owing to its dead weight, will

be inclined to the trailing edge. On this basis, this study proposes an optimized monitoring

methodology to closely monitor the pore-water pressure, rainfall, and landslide frontal

displacement during monsoon, proposed method focuses on the overall inclination angle change

of the plate girder during the non-rainy season.

Acknowledgments

We thank Dr. Long Chen at the Institute of Exploration Technology of CAGS for providing landslide monitoring data. This work was supported by the National Natural Science Foundation of China (41804089), Project of Observation Instrument Development for Integrated Geophysical Field of China Mainland (Y201802), and CGS of China Geological Survey Project (1212011220169 and 12120113011100).

References

Barlow, J., Martin, Y., Franklin, S. E.: Detecting translational landslide scars using segmentation of Landsat ETM+ and DEM data in the northern Cascade Mountains, British Columbia, Canadian Journal of Remote Sensing, 29(4):510-517, 2003.

Bellanova, J., Calamita, G., Giocoli, A., Luongo, R., Piscitelli, S.: Electrical resistivity imaging for the characterization of the Montaguto landslide(southern Italy), Engineering Geology, 243(1):272-281, 2018.

Brown, E., Hoek, E.: Trends in relationships between measured in-situ stresses and depth. International Journal of Rock Mechanics and Mining Sciences & Geomechanics Abstracts, 15(4):78-85, 1978.

Chen L., Liu Y., Feng X.: The investigation report on remediation project of Wobaoshi landslide, Sanhui Town, Enyang District, Bazhong City, The Institute of Exploration Technology of CAGS, Chengdu, Open File Rep., 57-75, 2015.

547   Cruden, D.M., Varnes, D.J.: Landslide Types and Processes, Special Report , Transportation Research

548   Board, National Academy of Sciences, 247:36-75, 1996.

549   Darve F., Vardoulakis I.: Degradations and Instabilities in Geomaterials, Springer Vienna, Austria,

550   2004.

551   Emelyanova E.II.: The basic rule of landslide movement, Chongqing Publishing House, Chongqing,

552   China, 1986.

553   Fan, X., Xu, Q., Zhang, Z., et al: The genetic mechanism of a translational landslide, Bulletin of

554   Engineering Geology and the Environment, 68(2):231-244, 2009.

555   Fan, X.: Mechanism and remediation measures for translational landslide [M. S. Thesis], Chengdu:

556   Chengdu University of Technology, 2007.

557   Fan X., Xu Q., Zhang Z., et al: Study of genetic mechanism of translational landslide, Chinese Journal

558   of Rock Mechanics and Engineering, 27(Supp.2):3753-3759, 2008.

559   Floris M., Bozzano F.: Evaluation of landslide reactivation: a modified rainfall threshold model based

560   on historical records of rainfall and landslides, Geomorphology, 94(1-2): 40-57, 2008.

561   Griffiths, D. V., Lane, P. A.: Slope stability analysis by finite elements, Géotechnique, 49(3), 387-403,

562   1999.

563   Guzzetti, F., Cardinali, M., Reichenbach P., et al.: Landslides triggered by the 23 November 2000

564   rainfall event in the Imperia Province, Western Liguria, Italy, Engineering Geology,

565   73(3-4):229-245, 2004.

566   Guo X., Huang R., Deng H., Xu Q., ZHAI G.: Formation and mechanism analysis of multi-level rift

567   trough in translational sliding landslide, Journal of Engineering Geology, 21(5):770-778, 2013.

568   Kong J., Chen Z.: The translational landslide in red stratum located in east of Sichuan in July, 1989.

569   Beijing: China Railway Publishing House, Landslide Column(9), 1989.

570   Labuz J. F., Zang A.: Mohr–Coulomb Failure Criterion, Rock Mechanics and Rock Engineering,

571   (2012)45:975–979, 2012.

572   Lin J. Yang W., Bao C.: Progressive collapse mechanism of hybrid structures with different vertical

573   stiffness, China Earthquake Engineering Journal, 40(4):713-720, 2018.

574   Liu Y., Wang J.: The research and application of landslide surface crack monitoring method based on

575   laser ranging mode, Environmental and Earth Sciences Research Journal, 2(2):19-24, 2015.

576   Martin, Y. E., Franklin, S. E.: Classification of soil- and bedrock-dominated landslides in British

577   Columbia using segmentation of satellite imagery and DEM data, International Journal of

578   Remote Sensing, 26(7):1505-1509, 2005.

579   Matjaž, M., Matja, C., Mitja, B.: Hydrologic conditions responsible for triggering the Stože landslide,

580   Slovenia, Engineering Geology, 73(3-4):193-213, 2004.

581   Sergio, D. N., Lourenco, K. S., Hiroshi, F.: Failure process and hydrologic response of a two layer

582   physical model: Implications for rainfall-induced landslides, Geomorphology, 73(1-2):115-130,

583   2006.

584   Teixeira, M., Bateira, C., Marques, F., et al: Physically based shallow translational landslide

585   susceptibility analysis in Tibo catchment, NW of Portugal, Landslides, 12(3):455-468, 2015.

586   Tschuchnigg, F., Schweiger, H.F. & Sloan, et al: Slope stability analysis by means of finite element

587   limit analysis and finite element strength reduction techniques. Part I: Numerical studies

588   considering non-associated plasticity, Computers and Geotechnics, 70, 169-177, 2015.

589   Tschuchnigg, F., Schweiger, H.F., Sloan, S.W., et al: Comparison of finite-element limit analysis and

590   strength reduction techniques, Géotechnique, 65(4), 249-257, 2015.

591   Wang L.,Zhang Z.: The mechanical patterns of the deformation in rock slope, Geological Publishing

592   House, Beijing, China, 1985.

593   Xu Q., Zeng Y.: Research on acceleration variation characteristics of creep landslide and early-warning

594   prediction indicator of critical sliding, Chinese Journal of Rock Mechanics and Engineering,

595   28(6):1099-1106, 2009.

596   Xu Q., Huang R., Liu T., et al.: Study on the formation mechanism and design of control engineering

597   for the super-huge Tiantai landslide, Xuanhan County, Sichuan Province, China, IAEG2006

598   Engineering Geology for Tomorrow Cities, Sichuan province, China, 2006.

599   Xu Q., Fan X., Li Y., Zhang S.: Formation condition, genetic mechanism and treatment measures of

600   plate-shaped landslide, Chinese Journal of Rock Mechanics and Engineering, 29(2):242-250,

601   2010.

602   Yin K., Jian W., Zhou C., et al: Study on the mechanism of the translational landslide in Wanzhou

603   district and prevention project, Wuhan: China University of Geosciences,Open File,

604   pp.153-154, 2005.

605   Zhang L., Pei X., Lin H., Li S.: Evolution of Landslide Based on Growth Characteristics of Trees on

606   the Landslide, Mountain Research, 33(4):503-510, 2015.

607   Zhang Z., Wang S., Wang L.: The analytical principle on engineering geology, Geological Publishing

608   House, Beijing, China, 1994.

Figure Captions

Fig. 1. Geographical location and elevation map of the Wobaoshi landslide.

Fig. 2. Topographic map of the Wobaoshi landslide and photographs of observation points: (a) exposed bedrock at the front edge; (b) the houses had cracked at the front edge (c) the roadbed is pushed uplifted at the front edge; (d) crack II and bent trees; and (e) crack I.

Fig. 3. I- I′ sectional graph of the landslide.

Fig. 4. Layout planar graph of the monitoring equipment.

Fig. 5. Photos of installation the monitoring instruments: (a) crack I gauge; (b) rain gauge and pore-water pressure gauge; and (c) crack II gauge.

Fig. 6. Monitoring data curves (rainfall intensity and width of cracks I and II).

Fig. 7. Monitoring data curves: (a) width of crack I and its pore-water pressure; (b) width of crack II and its pore-water pressure.

Fig. 8. Absolute slippage amount curves of cracks I and II.

Fig. 9. Geomechanical model of two-stage plate-shaped sliding bodies.

Fig. 10 Determination of the maximum measured pore-water level $h_{cr}^{'}$.

Fig. 11. Comparison figure of $h_{cr}^{'}$ (measured) and h_{cr} (theoretical).

Fig. 12 Example of finite element simulation and numerical calculation.

Fig. 13 Schematic of the deformation and failure mode of the Wobaoshi landslide.

Table

Table 1   Typical monitoring data of the Wobaoshi landslide

Measurement duration	Crack I width (m)	Crack II width (m)	Crack I Pore-water pressure (kPa)	Crack II Pore-water pressure (kPa)
2015/2/1	5.640	4.492	0	0
2015/4/24	5.945	4.774	18.561	27.303
2015/5/7	5.886	4.798	18.649	33.212
2015/5/13	6.203	4.810	33.134	33.036
2015/5/15	6.215	4.899	34.476	35.456
2015/8/15	6.350	5.451	41.474	31.625
2015/9/14	6.330	5.380	34.594	30.772
2015/11/15	5.871	4.952	11.280	17.395
2016/2/15	5.790	4.599	0	0
2016/4/13	5.824	4.706	10.378	26.156
2016/5/14	6.173	4.850	33.810	36.035
2016/7/17	6.161	5.281	36.162	31.664
2016/8/18	6.310	5.220	38.024	33.683
2016/9/15	6.325	5.251	39.298	29.723
2016/12/20	5.960	4.763	5.106	0
2017/2/16	5.865	4.770	0	0
2017/4/13	5.984	5.152	24.108	29.155
2017/5/17	6.118	5.332	43.463	31.703
2017/7/17	6.433	5.239	42.787	30.478
2017/8/15	6.490	5.255	43.639	29.273
2017/11/14	6.091	5.004	5.488	8.428
2017/12/20	5.922	4.723	0	0
2018/1/11	5.881	4.751	0	0
2018/4/10	6.194	5.110	33.957	35.819
2018/5/17	6.283	5.246	33.830	33.438
2018/6/16	6.452	5.315	36.995	28.391
2018/7/10	6.421	5.310	38.171	29.841

Table 2   Rainfall intensity value of the Wobaoshi landslide (mm/month)

Year \ Month	1	2	3	4	5	6	7	8	9	10	11	12	Total
2015		13.5	30.5	71.8	121.9	165.0	240.1	163.0	166.1	85.0	39.6	14.1	1110.6
2016	6.9	12.5	26.5	56.8	98.4	126.1	193.2	155.1	150.0	90.3	29.1	13.5	958.4
2017	5.7	16.8	36.8	90.5	115.6	185.1	271.3	190.0	176.2	109	52.1	20.8	1269.9
2018	11.5	10.9	31.5	99.9	121.0	205.1	191.6	\	\	\	\	\	671.5

634

Table 3 Measured pore-water level data of the sliding bodies

Measured time	Crack Ⅰ slippage (m)	Measured pore-water level (m)	Crack Ⅱ slippage (m)	Measured pore-water level (m)
2015/4/15	0.072	14.566	0.183	12.736
2015/4/24	0.305	15.174	0.282	12.936
2015/5/7	0.246	15.183	0.306	13.539
2015/5/13	0.561	16.661	0.318	13.521
2015/5/15	0.573	16.798	0.407	13.768
2015/6/20	0.711	17.032	0.888	13.502
2015/7/17	0.519	17.474	0.798	13.471
2015/10/16	0.481	16.470	0.538	13.340
2015/11/15	0.229	14.431	0.458	11.925
2016/1/15	0.108	\	0.169	\
2016/4/13	0.184	13.490	0.214	12.819
2016/4/23	0.421	14.339	0.269	12.804
2016/4/29	0.475	16.214	0.432	13.835
2016/5/11	0.469	16.494	0.449	13.920
2016/5/14	0.531	16.505	0.358	13.827
2016/6/15	0.508	16.731	0.618	13.574
2016/9/15	0.683	17.312	0.758	13.183
2016/10/12	0.637	14.930	0.618	12.360
2017/2/16	0.223	\	0.278	\
2017/4/13	0.344	15.741	0.658	13.125
2017/4/29	0.489	16.712	0.686	13.141
2017/5/2	0.518	16.799	0.648	13.024
2017/5/13	0.501	16.877	0.734	13.161
2017/5/17	0.476	17.715	0.838	13.385
2017/8/15	0.848	17.733	0.758	13.137
2017/9/16	0.869	16.324	0.333	12.235
2018/3/14	0.281	\	0.618	11.013
2018/4/10	0.552	16.745	0.754	13.805
2018/5/17	0.643	16.732	0.333	13.562

635

636

Table 4 Mechanical parameters of the sliding body model

Lithology	Elastic Modulus (N/m^2)	Poisson Ratio	Unit Weigth (N)	Internal Cohesion (N/m^2)	Internal Friction Angle	Permeability Coefficient (cm/s)
Arkose	600000	0.25	19200	30000	36°	1.20E-07
Silty Mudstone	360000	0.28	19000	20000	30°	6.00E-07
Clay	300000	0.3	18000	10200	11.2°	1.20E-06

637

638

639

Table 5   Loading steps of the water level in Crack I and II in FEM model

Loading Steps	Crack I	Crack II
0	314.50 m	311.00 m
1	316.00 m	313.00 m
2	317.50 m	315.00 m
3	316.00 m	313.00 m
4	314.50 m	311.00 m

640